

Cite this: *J. Mater. Chem. A*, 2021, 9, 5475

An exceptionally large energy cathode with the K–SO₄–Cu conversion reaction for potassium rechargeable batteries†

Yongseok Lee,^a Jung-Keun Yoo,^c Hyunyoung Park,^b Wonseok Ko,^a Jungmin Kang,^{ab} Jae Hyeon Jo,^d Gabin Yoon,^e Hyeon-Gyun Im,^f Hitoshi Yashiro,^g Seung-Taek Myung^{ib} and Jongsoo Kim^{id}*^{ab}

Although layered-type cathode materials for lithium-ion batteries (LIBs) have received great attention due to their large gravimetric energy density, those for potassium rechargeable batteries (PRBs) just deliver small and limited energy density due to the large structural change and phase transition during de/intercalation of K⁺ ions with a large ionic size. Thus, a new approach is required for achieving high energy densities. A cathode material that results in ultrahigh energy density for potassium rechargeable batteries (PRBs) based on the conversion reaction of K–SO₄–Cu in the system was developed. To maximize the electrochemical performance, a copper-sulfate/carbon nanocomposite (hereafter denoted as N-CSO/C) was prepared using a simple high-energy ball-milling process. At a current density of 12 mA g⁻¹, the conversion reaction of K–SO₄–Cu in the PRB system resulted in a specific capacity of ~240 mA h g⁻¹ with an average operating voltage of ~2.8 V (vs. K⁺/K). This capacity and the resulting energy density are larger than those of other cathode materials for PRBs reported to date. After 200 cycles at 360 mA g⁻¹, N-CSO/C retained ~70% of the initial capacity. The overall reversible reaction mechanism of K–SO₄–Cu in N-CSO/C in the PRB system was investigated through combined studies using first-principles calculation and various experimental techniques.

Received 20th October 2020
Accepted 13th November 2020

DOI: 10.1039/d0ta10234b

rsc.li/materials-a

1. Introduction

Environmental problems such as air pollution or fine dust from the abuse of fossil fuels have been considered some of the most serious issues in the world.^{1,2} Thus, developing energy storage systems (ESSs) has received great attention for efficient usage of eco-friendly and sustainable energy. Among the various ESSs, Li-ion batteries (LIBs) are considered promising because of their outstanding electrochemical properties with high energy

density and stable cycle performance.^{3,4} Thus, the application range of LIBs has been enlarged from small electronic devices to grid-scale ESSs.^{5,6} However, the ongoing depletion of the limited Li resources on earth and the resulting increase of the LIB production cost may not satisfy the explosive growth in the global demand of LIBs, which may restrict further application of LIBs in industries.^{7–11} Thus, despite the undeniable merits of LIBs, it is necessary to develop alternative ESSs that use elements that are more abundant on earth.

Recently, potassium rechargeable batteries (PRBs) have received great attention as promising alternatives to lithium-ion batteries (LIBs) for large-scale applications owing to not only the abundant potassium resources in the earth but also the lower redox potential of potassium metal relative to that of other alkali(-earth) metals (K⁺/K: –2.93 V vs. the standard hydrogen redox potential (SHE); Na⁺/Na: –2.71 V vs. SHE, and Mg²⁺/Mg: –2.27 V vs. SHE).^{12,13} Moreover, it was reported that K⁺ ions as well as Li⁺ ions are reversibly de/intercalated in graphite-type materials which are considered some of the most suitable anode electrodes for commercialized LIBs,¹⁴ which indicates that graphite-type materials can be used as promising anodes for PRBs. Thus, the established industrial facilities for producing graphite-type materials as LIB anodes can be more smoothly applied for the PRB system than for other rechargeable batteries.¹⁵ Thus, it is expected that established systems for

^aDepartment of Nanotechnology and Advanced Materials Engineering, Sejong University, Seoul, 05006, Republic of Korea. E-mail: jongsookim@sejong.ac.kr

^bDepartment of Energy Science, Sungkyunkwan University, Suwon, 16419, Republic of Korea. E-mail: jongsookim@skku.edu

^cCarbon Composites Department, Composites Research Division, Korea Institute of Materials Science (KIMS), 797 Changwondaero, Changwon, Republic of Korea

^dNew Energy Laboratory, Korea Electronic Power Research Institute, Daejeon, 34056, South Korea

^eNext Generation Battery Lab, Samsung Advanced Institute of Technology, 130 Samsung-ro, Yeongtong-gu, Suwon-si, Gyeonggi-do 16678, Republic of Korea

^fInsulation Materials Research Center, Electrical Materials Research Division, Korea Electrotechnology Research Institute (KERI), Chang Won, 51543, Republic of Korea

^gDepartment of Chemistry and Bioengineering, Iwate University, 4-3-5 Ueda, Morioka, Iwate 020-8551, Japan

† Electronic supplementary information (ESI) available: Supplementary Fig. x and tables. See DOI: 10.1039/d0ta10234b

LIBs can be more easily applied for PRBs than for other rechargeable battery systems. Studies on PRBs have focused on intercalation-based cathode materials with outstanding electrochemical performance. Layered-type materials in particular have attracted attention as promising cathode materials for PRBs owing to their large theoretical gravimetric energy density.^{16–18} Unlike the layered-type cathode materials for LIBs, however, most of the layered-type cathode materials for PRBs such as O3-, P2-, and P3-type K_xMO_2 (M: transition metal) exhibit specific capacities less than 130 mA h g^{-1} even at low current densities in the available voltage range.^{19–21} Thus, we speculate that rather than an intercalation-based reaction, another reaction mechanism will be required for the development of novel cathode materials for PRBs with large specific capacities of more than 200 mA h g^{-1} .²¹ Conversion-based electrode materials are generally applied as the anode for rechargeable batteries because of the low average operating voltages of less than 0.5 V despite their large specific capacities compared with those of intercalation-based cathode materials.^{22–25} We speculated that the limited energy densities of intercalation-based cathode materials for PRBs could be overcome by focusing on the development of novel conversion-based cathode materials with high operating voltage. Our strategy to increase the operating voltage for the conversion reaction is to maximize the inductive effect arising from polyanion groups in the structure.^{26–28}

In this work, we prepared a copper-sulfate/carbon nanocomposite (hereafter denoted as N-CSO/C) as a novel conversion-based cathode material for PRBs. The conversion reaction of $K-SO_4-Cu$ in the PRB system resulted in a large specific capacity of $\sim 240 \text{ mA h g}^{-1}$ and an average operating voltage of $\sim 2.8 \text{ V}$ (vs. K^+/K) at 12 mA g^{-1} ; the resulting energy density is the largest among those of cathode materials for PRBs reported to date. Even at a current density of 1080 mA g^{-1} , N-CSO/C maintained a specific capacity of $\sim 170 \text{ mA h g}^{-1}$, which corresponds to $\sim 70\%$ of the capacity at 12 mA g^{-1} . Furthermore, after 200 cycles at a current density of 360 mA g^{-1} , N-CSO/C retained $\sim 70\%$ of the initial capacity. Through combined studies using first-principles calculation and various *operando/ex situ* techniques, including X-ray diffraction (XRD), high-resolution transmission electron microscopy (HRTEM), time-of-flight secondary-ion mass spectroscopy (ToF-SIMS), X-ray absorption near edge structure (XANES) spectroscopy, and extended X-ray absorption fine structure (EXAFS) spectroscopy, we confirmed the following reversible conversion reaction mechanism in N-CSO/C during charge/discharge: $CuSO_4 + 2K^+ + 2e^- \leftrightarrow Cu + K_2SO_4$.

2. Experimental

2.1 Preparation of N-CSO/C

To prepare pure $CuSO_4$ powder, copper(II) sulfate $\cdot 5H_2O$ (Sigma Aldrich, 98%) was heated at $500 \text{ }^\circ\text{C}$ for 5 h in air. The $CuSO_4$ became whitish-gray after dehydration and was then mixed with conductive carbon by high-energy ball milling 80 wt% $CuSO_4$, 19 wt% Super P carbon black and 1 wt% carbon nanotubes (CNTs). The powders were placed in a nitride jar with 30 balls

and ball milled at 500 rpm for 12 h, in order to prepare the N-CSO/C nanocomposite.

2.2 Materials characterization

The N-CSO/C powders were characterized using XRD (PANalytical) with $Cu K\alpha$ radiation (wavelength = 1.54178 \AA). The 2θ range was $10\text{--}60^\circ$ with a time per step of 0.13 s. The FullProf Rietveld program was used to analyze the XRD data. The morphology of the materials was examined using SEM (SU-8010). The overall conversion reaction was evaluated using HR-TEM (JEM-3010) at the National Center for Inter-university Research Facilities (NCIRF) at Seoul National University. XANES spectroscopy was performed at beamline 10C at the 3.0 GeV Pohang Light Source. The electrodes were tested using a time-of-flight secondary ion mass spectroscopy (ULVAC-PHI, ToF-SIMS PHITRIFT V nanoTOF) surface analyser to identify the byproducts on the surface of the active materials. The analyser operated at 10^{-9} Torr, and the liquid Ga^+ ion source and pulse electron flooding were equipped. For the ToF-SIMS measurements, a Liquid Metal Ion Gun (LMIG) was used as the primary ion source and there are three types of ion sources for the LMIG; Ga, Au and Bi. Au and Bi ion beams contain a lot of polymer ions, which is appropriate for high-mass molecules; therefore, the two element beams are usually used to measure molecules. Meanwhile, the Ga ion beam consists of monomers, which is appropriate for low-mass areas, mainly elements. The active material targets were bombarded by 10 keV Ga^+ beams from 0.3 to 0.5 pA of a pulsed primary ion current during the analysis. *Operando* XRD patterns of N-CSO/C were obtained using an XRD diffractometer (PANalytical, Empyrean) with $Cu K\alpha$ radiation ($\lambda = 1.54178 \text{ \AA}$) in the 2θ range of $27\text{--}45^\circ$ using a step size of 0.026° . During the *operando* XRD experiments, we used an *operando* battery cell (ISBC) for XRD made by PANalytical with PDC TECH. The cell was measured at 12 mA g^{-1} in the voltage range of 1.5–4.1 V with a K counter electrode, a separator (Celgard 2400), and 0.5 M KPF_6 in EC : DEC = 1 : 1 (v/v) as the electrolyte. A beryllium (Be) window was used to protect the cell system from water.

2.3 Electrochemical characterization

The electrodes were fabricated from a slurry of 87.5 wt% N-CSO/C composite, 2.5 wt% Super-P carbon, and 10 wt% polyvinylidene fluoride (PVDF) binder in *N*-methyl-2-pyrrolidone (NMP). Thus, the N-CSO/C electrode consisted of 70 wt% $CuSO_4$ as the active material, 20 wt% conductive carbon, and 10 wt% PVDF binder. For a fair comparison of the electrochemical performance of the N-CSO/C and pristine $CuSO_4$ electrodes, we applied the same mass ratio of 70 wt% $CuSO_4$, 20 wt% conductive carbon, and 10 wt% PVDF binder for the preparation of both electrodes. The slurry was applied on Al foil using a doctor blade and dried in an oven at $110 \text{ }^\circ\text{C}$ for 12 h. R2032 cells were assembled in an Ar-filled glove box using the $CuSO_4$ composite electrode, a K counter electrode, a separator (Celgard 2400), and 0.5 M KPF_6 in EC : DEC = 1 : 1 (v/v) as the electrolyte. The electrochemical performance of each cell was evaluated by charging and discharging in the voltage range of

1.5–4.1 V at 30 °C using an automatic battery charge/discharge test system (WBCS 3000, WonATech). The impedance of each sample was analyzed from 1 MHz to 500 mHz with a 10 mV amplitude using a multichannel impedance analyzer (VSP-300, Bio-Logic, Grenoble, France).

3. Results and discussion

3.1 Conversion-based cathode material with high operating voltage *via* the inductive effect

Fig. 1a shows the overall conversion reaction mechanism of $\text{KSO}_4\text{-Cu}$ in the PRB system. During discharge, the CuSO_4 phase disappears and then K_2SO_4 and metallic Cu^0 phases are newly formed at the same time. Then, the CuSO_4 phase is recovered by conversion reaction between K_2SO_4 and metallic Cu^0 phases during the charge process. In this conversion reaction of CuSO_4 in the PRB system, we expect that the presence of $(\text{SO}_4)^{2-}$ polyanions in the structure would maximize the inductive effect among Cu–O–S bonds, implying that CuSO_4 could deliver a high redox potential as a cathode for PRBs despite the conversion-based reaction, unlike other metal-oxide compounds (Fig. 1b). Polyanion-based materials are composed of not only M and O ions but also additional anions with high electronegativity. O ions in polyanion-based materials are shared by not only M ions but also the anions, which results in weakened bonding between O and M ions in the polyanion-based materials compared to the general metal-oxide materials. Thus, the gap between bonding and anti-bonding orbitals is reduced due to the existence of additional anions with high electronegativity.^{29,30} As a result, the redox reaction of M ions in polyanion-

based materials can occur at a higher operating voltage than that in the general metal-oxide materials. Moreover, it was reported that the $(\text{SO}_4)^{2-}$ -based materials can be capable of largely upshifting the redox potential through the inductive effect of sulfur with high electronegativity.³¹ For these reasons, we expected that the operating voltage of the conversion-based electrode materials can be increased by maximizing the induction effect of polyanions. We predicted the theoretical redox potentials for the polyanion CuSO_4 and the metal-oxide CuO in the PRB system using first-principles calculation (Table S1a (ESI[†])). The expected conversion reactions of (1) CuSO_4 and (2) CuO in the PRB system are as follows: (1) $\text{CuSO}_4 + 2\text{K}^+ + 2\text{e}^- \leftrightarrow \text{Cu} + \text{K}_2\text{SO}_4$ and (2) $\text{CuO} + 2\text{K}^+ + 2\text{e}^- \leftrightarrow \text{Cu} + \text{K}_2\text{O}$. Table S1b (ESI[†]) presents the formation energies for the species used to calculate the theoretical redox potentials of CuSO_4 and CuO in the PRB system. According to the calculation, CuSO_4 exhibits an average operating voltage of ~ 3.2 V (vs. K^+/K), which is higher than that of other conversion-based cathodes for PRBs. It was predicted that CuO delivers an average redox potential of ~ 1.7 V (vs. K^+/K). Through these analyses using first-principles calculations, we confirmed that the presence of polyanions with high electronegativity, such as $(\text{SO}_4)^{2-}$, results in a high operating voltage despite the conversion reaction. Furthermore, the theoretical capacity of CuSO_4 based on the conversion reaction mentioned above is ~ 360 mA h g^{-1} . These results based on first-principles calculations imply that CuSO_4 can deliver larger energy densities than other intercalation-based cathode materials for PRBs. In addition, we confirmed that CuSO_4 exhibits higher theoretical redox potential in the

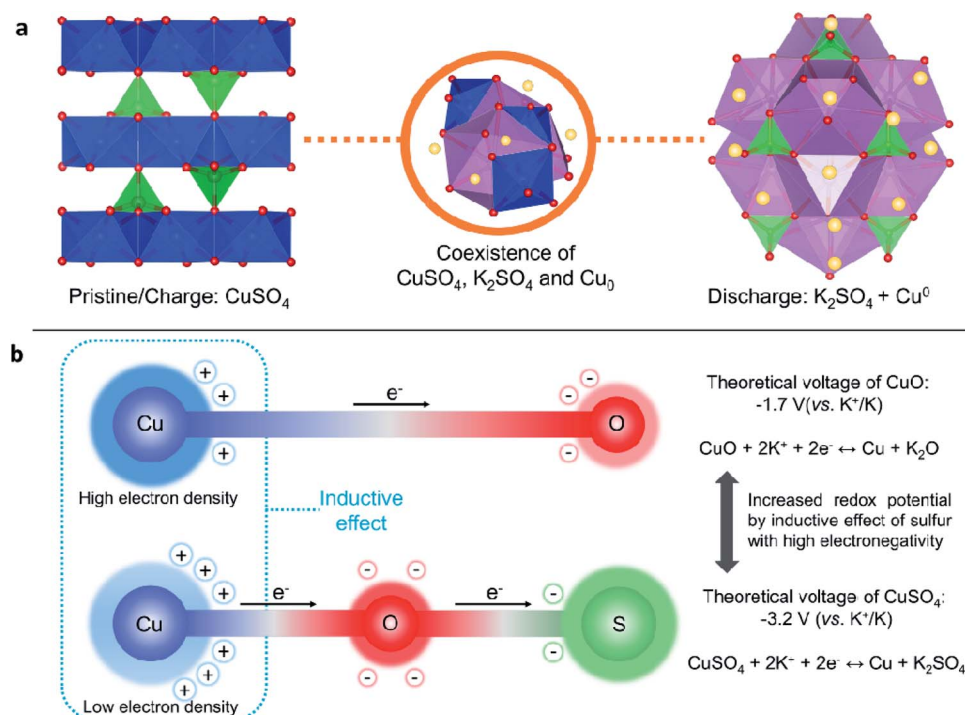


Fig. 1 (a) Scheme of the overall conversion reaction mechanism of CuSO_4 in the PRB system. (b) Scheme of the higher redox potential of CuSO_4 than of CuO arising from the inductive effect due to sulfur with high electronegativity.

PRB system than those of the Na-ion battery (NIB) and Mg-ion battery (MIB) systems (Table S2 (ESI[†])), which indicates the better suitability of CuSO₄ as the cathode for PRBs rather than NIBs or MIBs. To realize the theoretical electrochemical properties of CuSO₄ in the PRB system, we fabricated nano-sized CuSO₄ particles that were homogeneously mixed with conductive carbon using a simple high-energy ball-milling process (Fig. S1 (ESI[†])). It has been reported that the long ion-diffusion length in conversion-based electrode materials leads to the poor electrochemical performance; thus, shortening the ion path is essential for these materials.^{32,33} Furthermore, the application of a homogeneous conductive carbon coating on the surface of particles can enhance the electrical conductivity and act as a buffer that prevents the destruction of the crystal structure during charge/discharge.³⁴ We thus speculated that the high-energy ball-milling process would allow us to successfully achieve these two goals simultaneously.

3.2 Morphology and crystal structure of N-CSO/C

Scanning electron microscopy (SEM) was used to compare the particle sizes of the as-prepared CuSO₄ and N-CSO/C (Fig. 2a and b). The overall particle size of CuSO₄ was greatly decreased by pulverization through high-energy ball milling. Moreover, the intensities and full width at half maximum (FWHM) of the XRD peaks for the CuSO₄ phase substantially changed after high-energy ball milling (Fig. 2c), indicating a difference in the crystallite size between the as-prepared CuSO₄ and N-CSO/C. Using the Scherrer equation, we calculated the crystallite sizes of the as-prepared CuSO₄ and N-CSO/C from their XRD patterns

(Fig. 2d and e). The average crystallite size of N-CSO/C was only ~9.86 nm, which was smaller than that of the as-prepared CuSO₄ (~33.37 nm). In addition, Rietveld refinement analyses on N-CSO/C based on the XRD data revealed that N-CSO/C possessed a pure orthorhombic crystal structure with the *Pnma* space group without any impurities such as copper carbide or second phases, despite the high-energy ball-milling with conductive carbon (Fig. 3a). The calculated lattice parameters of N-CSO/C were determined to be $a = 8.4090(6)$ Å, $b = 6.7005(3)$ Å, $c = 4.8176(3)$ Å, and $\beta = 90^\circ$, which agreed well with previously reported values in the literature (Table S3 (ESI[†])).³⁵ Moreover, homogeneous carbon mixing with CuSO₄ particles in N-CSO/C was confirmed through transmission electron microscopy (TEM) analyses and energy-dispersive X-ray spectroscopy (EDS) elemental mapping (Fig. 3b). The total carbon content in N-CSO/C was determined to be ~20 wt% by thermogravimetric analysis (TGA) (Fig. S2, (ESI[†])).

3.3 Electrochemical properties of N-CSO/C in the KIB system

Fig. 4a and b present the charge/discharge capacities of the N-CSO/C nanocomposite at various current densities in the voltage range of 1.5–4.1 V (*vs.* K⁺/K). For the full conversion reaction, the nanocomposite was initially discharged to 1.1 V (*vs.* K⁺/K). Fig. S3 (ESI[†]) shows the initial charge/discharge curve dQ/dV profile of the N-CSO/C nanocomposite. It was verified that the plateau region is partially found at the initial charge/discharge and dQ/dV profiles. Interestingly, N-CSO/C delivered a specific capacity of ~240 mA h g⁻¹ with an average operating voltage of ~2.8 V (*vs.* K⁺/K) at 12 mA g⁻¹; this

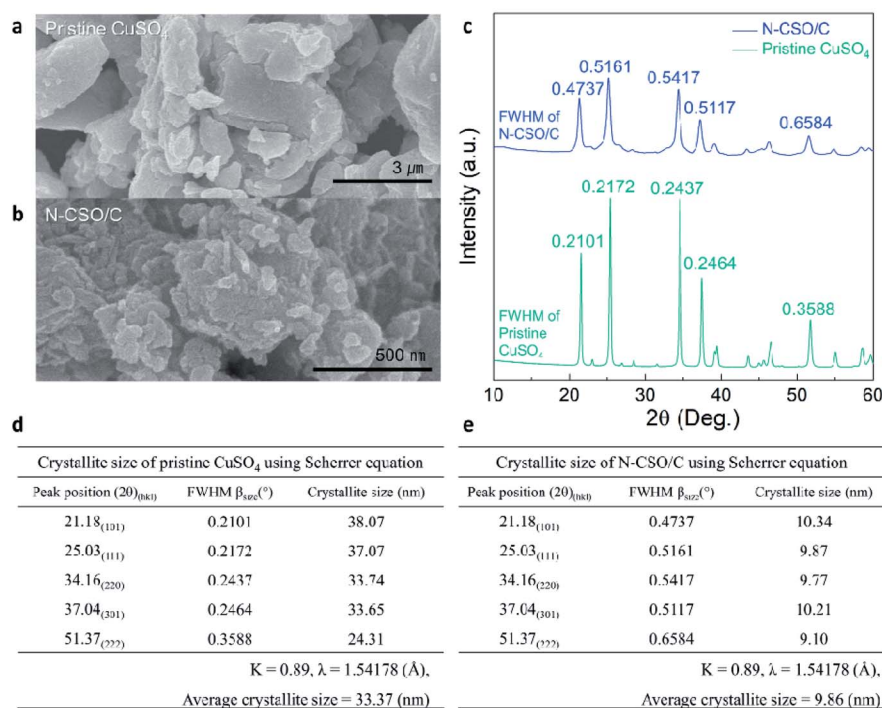


Fig. 2 SEM image of (a) pristine CuSO₄ and (b) N-CSO/C. (c) Intensities and FWHM of XRD peaks of the N-CSO/C composite and pristine CuSO₄. Crystallite size of (d) pristine CuSO₄ and (e) the N-CSO/C composite determined using the Scherrer equation for selected *hkl* reflections of the XRD patterns.

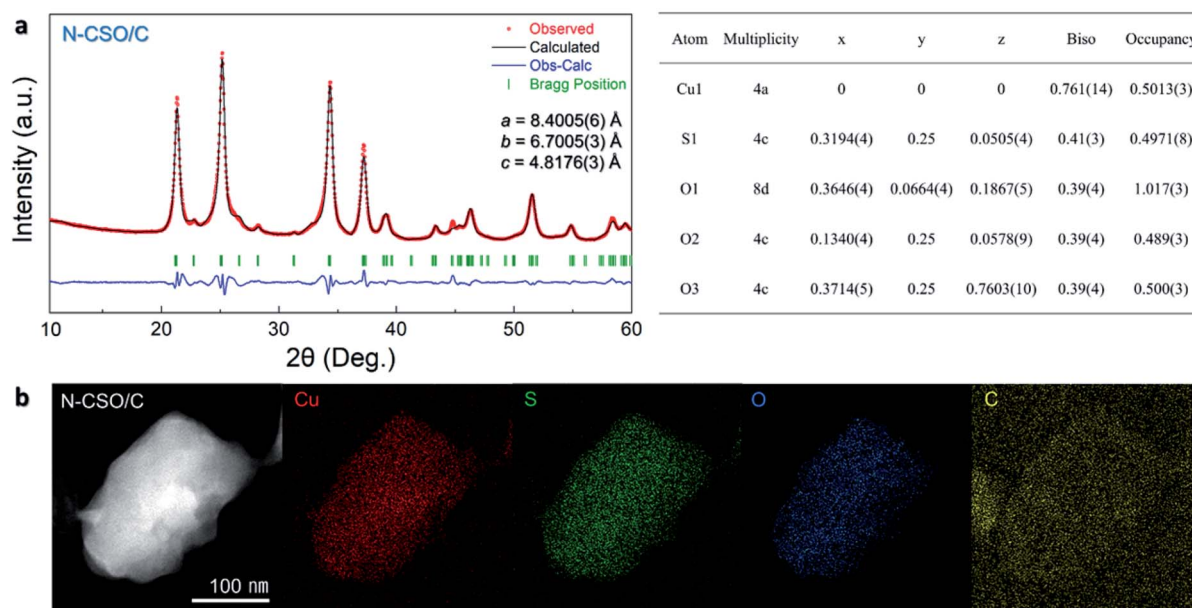


Fig. 3 (a) Rietveld refinement of the XRD pattern of N-CSO/C ($R_p = 3.64\%$, $R_1 = 1.98\%$, and $R_F = 2.12\%$) and the crystal structure of the N-CSO/C composite. (b) EDS elemental mapping of the N-CSO/C composite (Cu: red, S: green, O: blue, and C: yellow).

capacity and the resulting energy density are larger than those of other cathode materials for PRBs. Even at 1080 mA g^{-1} , N-CSO/C delivered a specific capacity of $\sim 170 \text{ mA h g}^{-1}$, corresponding to $\sim 70\%$ of the capacity measured at 12 mA g^{-1} . In

addition, it was supposed that the slope of the discharge curve at a high current density of 1800 mA g^{-1} is decreased compared to those at other low current densities because of the increased overpotential of the conversion reaction. After 200 cycles at

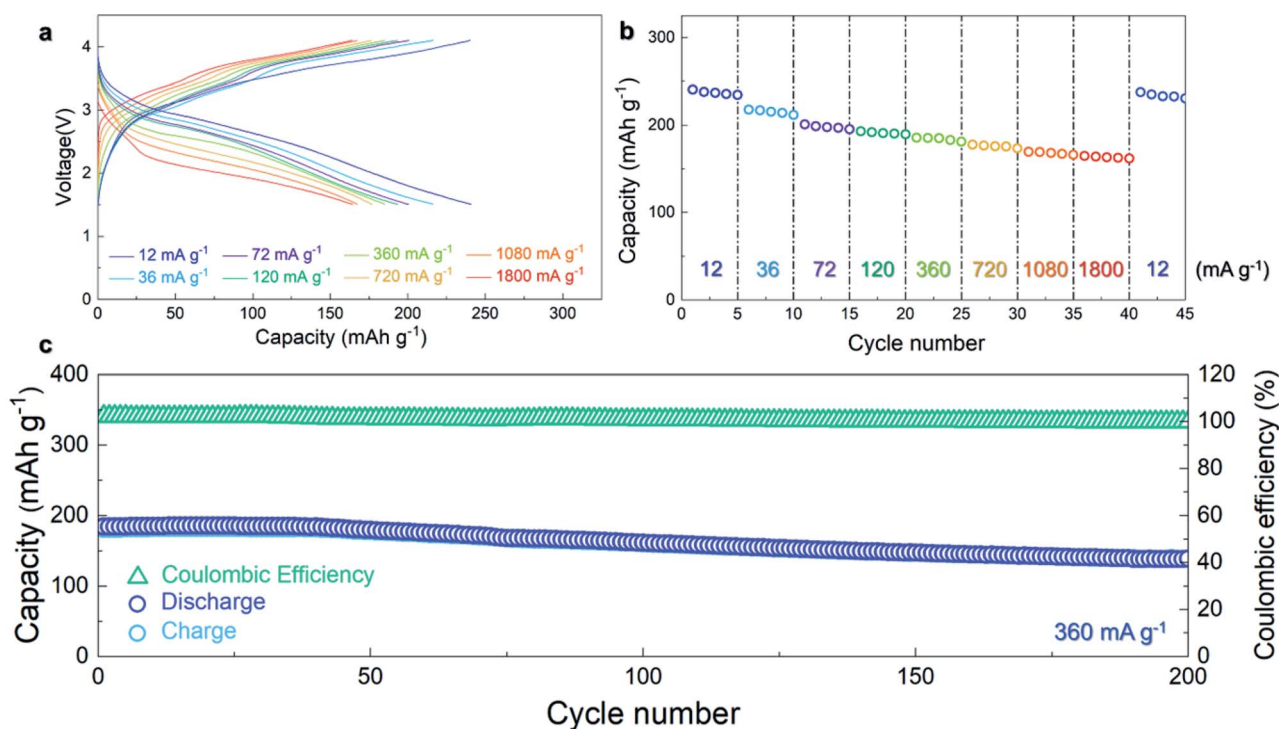


Fig. 4 (a) Charge/discharge curves of N-CSO/C at various current rates in the voltage range of 1.5–4.1 V (vs. K^+/K). (b) Rate cycling performance of the N-CSO/C composite from 12 to 1800 mA g^{-1} . (c) Cycling performance and coulombic efficiency of N-CSO/C over 200 cycles at 360 mA g^{-1} after 1 cycle at 120 mA g^{-1} .

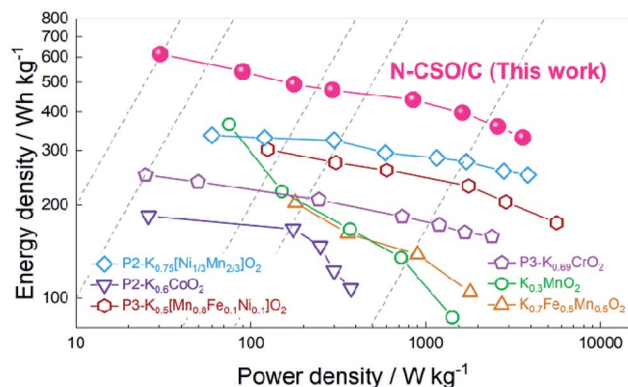


Fig. 5 Ragone plot of N-CSO/C and other cathode materials for PRBs (vs. K^+/K).

360 mA g^{-1} , N-CSO/C retained $\sim 70\%$ of its initial capacity (Fig. 4c), which is related to the well-retained crystal structure and morphology of N-CSO/C after 200 cycles (Fig. S4 (ESI †)). Moreover, Fig. S5 (ESI †) presents the cyclic voltammetry (CV) profiles of N-CSO/C at 1 mV s^{-1} . In addition, Fig. 5 shows that the outstanding electrochemical performance of N-CSO/C in the PRB system is clearly revealed through comparison with that of other cathodes for PRBs. It was reported that like the N-CSO/C nanocomposite, numerous cathode materials for PRBs are discharged to 1.5 V (vs. K^+/K) in the half-cell system with K metal for realization of their optimal electrochemical properties.^{16,36–40} These results imply the strong possibility of the application of N-CSO/C as a promising cathode for practical PRBs.

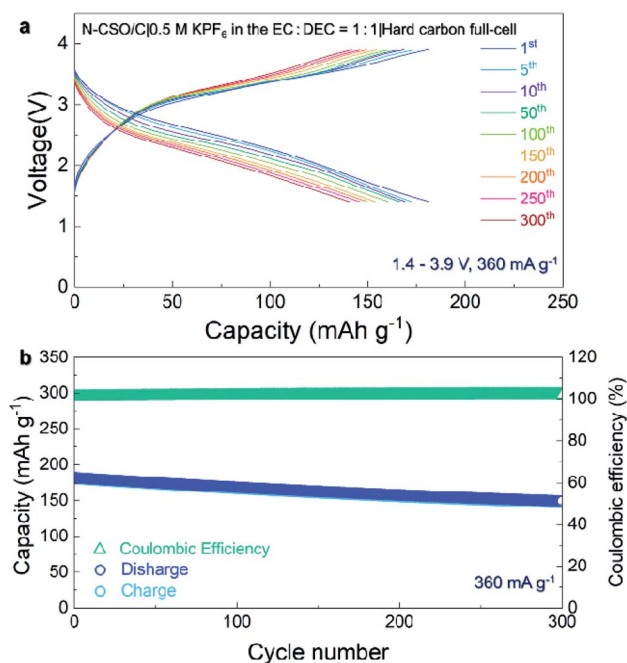


Fig. 6 (a) Charge/discharge profiles of the N-CSO/C|Hard-carbon full-cell at the 1st, 5th, 10th, 50th, 100th, 150th, 200th, 250th and 300th cycles. (b) Cycling performance and coulombic efficiency of the N-CSO/C full cell over 300 cycles at 360 mA g^{-1} .

Fig. 6 and Table S4 (ESI †) show that the N-CSO/C|Hard carbon full-cell delivered a large initial capacity of $\sim 202 \text{ mA h g}^{-1}$ at a current density of 360 mA g^{-1} and a highly stable cycle performance with $\sim 85\%$ capacity retention compared with the initial capacity over 300 cycles, indicating the high possibility of the application of N-CSO/C as a cathode for practical PRBs.^{16,36,37,41–44} In addition, the electrochemical properties of the full cell were analyzed in the voltage range of $1.0\text{--}4.0 \text{ V}$. It was reported that a number of full-cells for PRBs were tested at a discharge cut-off voltage of less than 1 V ,^{15,36,37,40,41} which indicates that the full-cell performances of the N-CSO/C composite tested in the voltage range between 1.0 and 4.0 V are competitive with those of other cathode materials for PRBs using the pre-cycled anodes. As shown in Fig. S6, † the hard carbon electrode was pre-cycled in the voltage range of $0.01\text{--}2.0 \text{ V}$ (vs. K^+/K) for two cycles to remove the irreversible capacity of the initial cycle. Moreover, to confirm the pre-cycling effect on the electrochemical performances of hard carbon as the PRB anode, we tested the full-cell performances of the N-CSO/C electrode using one-time and two-time pre-cycled hard carbon electrodes. Fig. S7, † shows that the full-cell performance using two-time pre-cycled hard carbon is more outstanding than that using one-time pre-cycled hard carbon. In addition, for the as-prepared CuSO_4 powder, its specific capacity at 12 mA g^{-1} was only $\sim 6 \text{ mA h g}^{-1}$ (Fig. S8 (ESI †)). Electrochemical impedance spectroscopy (EIS) analyses confirmed that the charge-transfer resistance of the as-prepared CuSO_4 was much larger than that of N-CSO/C (Fig. S9 (ESI †)). In addition, it is known that K^+ ion diffusion is more difficult than Li^+ ion diffusion owing to the larger ionic size of K^+ ($\sim 1.38 \text{ \AA}$) than of Li^+ ($\sim 0.76 \text{ \AA}$).¹⁷ Thus, because the conversion reaction between CuSO_4 and K^+ is accompanied by the sluggish kinetics, it was supposed that the N-CSO/C electrode delivers a relatively low specific capacity of $\sim 240 \text{ mA h g}^{-1}$ in the enlarged voltage range between 1.5 and 4.1 V (vs. K^+/K) compared to its theoretical capacity. Moreover, a specific capacity of $\sim 300 \text{ mA h g}^{-1}$ in the voltage range between 1.1 and 4.1 V (vs. K^+/K) in the initial cycle supports the sluggish kinetics of the CuSO_4 phase in the PRB system.

3.4 Demonstrating the conversion mechanism of N-CSO/C in the KIB system

The conversion reaction of $K\text{-SO}_4\text{-Cu}$ in the PRB system was evaluated using *operando* and *ex situ* XRD analyses (Fig. 7a, b and S10 (ESI †)). Although the entire phase of CuSO_4 disappeared during discharge to 1.1 V (vs. K^+/K), the growth of new XRD peaks at $29.8^\circ(2\theta)$, 30.8° , and 43.4° was detected, corresponding to the (013) and (211) planes of K_2SO_4 and the (111)

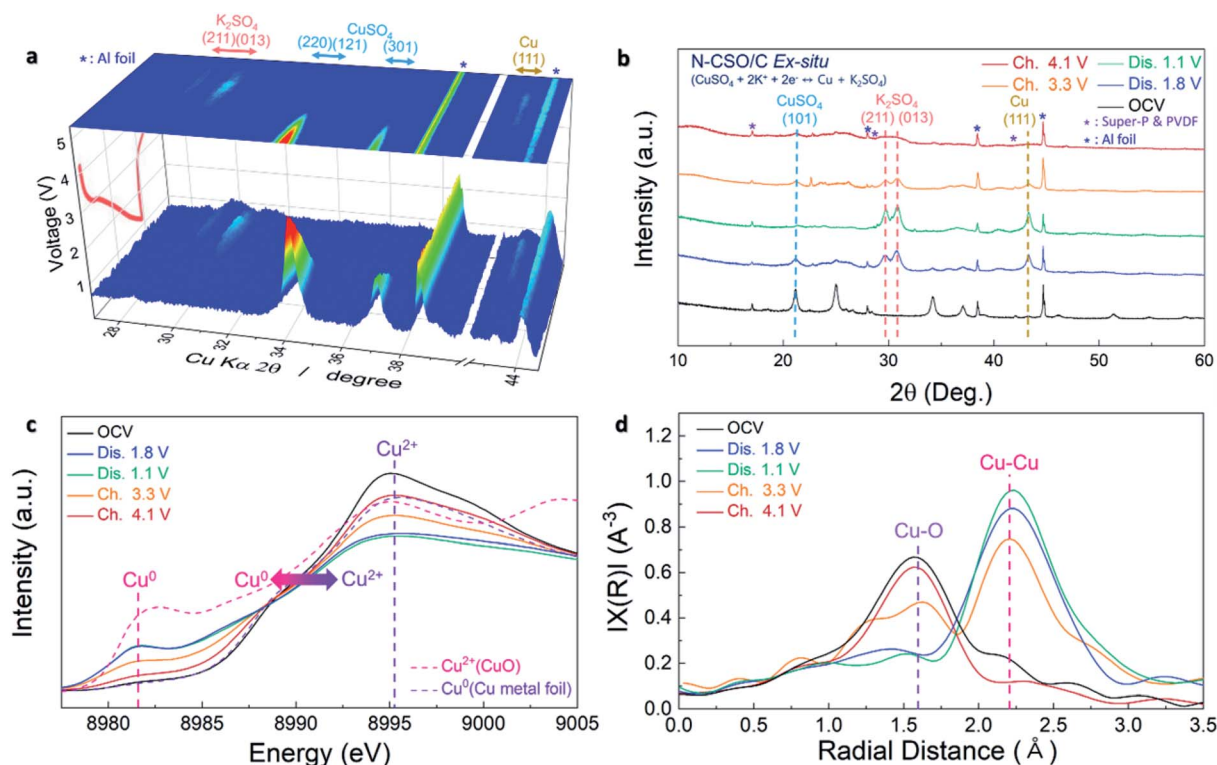


Fig. 7 (a) *Operando* XRD patterns of the N-CSO/C electrode during the first cycle. (b) *Ex situ* XRD patterns of N-CSO/C electrodes at various voltages. (c) XANES spectra and (d) EXAFS spectra of N-CSO/C electrodes.

plane of metallic Cu^0 , respectively. During charging to 4.1 V (vs. K^+/K), the intensities of the XRD peaks corresponding to the K_2SO_4 and metallic Cu^0 phases gradually declined, and the CuSO_4 phase with an amorphous or low-crystallinity structure was reversibly re-formed. Fig. S11 (ESI[†]) shows the *ex situ* XRD patterns of N-CSO/C electrodes with the expanded regions. In addition, these *operando/ex situ* XRD results are related to the well-defined slopes in the charge/discharge profiles of the N-CSO/C electrode without noticeable plateau regions after the initial cycle, which is consistent with the experimental results of the other conversion-based electrode materials for rechargeable batteries.^{47,48} These *operando* and *ex situ* XRD results indicate that the CuSO_4 phase in N-CSO/C undergoes a reversible conversion reaction during charge/discharge, as expressed by the following equation: $\text{CuSO}_4 + 2\text{K}^+ + 2\text{e}^- \leftrightarrow \text{Cu} + \text{K}_2\text{SO}_4$. There is no evidence of new compounds consisting of Cu^+ ions; the swift change of Cu^{2+} to metallic Cu^0 occurred without Cu^+ during the conversion reaction on CuSO_4 in the K-cell system. Moreover, it was verified that any impurities such as copper carbide were not formed during the charge/discharge process. In addition, to determine the change of the average oxidation states and local structure during charge/discharge, we performed XANES and EXAFS analyses on N-CSO/C from the as-prepared electrode to the fully charged/discharged electrodes (Fig. 7c and d).^{49,50} During discharge, the oxidation state of Cu changed from Cu^{2+} to metallic Cu^0 , as observed in the *ex situ* XANES spectra, and the peak intensity of the metallic Cu–Cu bond gradually increased with a weakened Cu–O bond, as

observed in the *ex situ* EXAFS spectra. For the fully charged N-CSO/C electrode, the oxidation state of Cu and the local structure were similar to those of the as-prepared N-CSO/C electrode. These results indicate the reversible conversion reaction from CuSO_4 to K_2SO_4 and metallic Cu^0 in the PRB system.

The conversion reaction of the CuSO_4 phase in the PRB system was also demonstrated through *ex situ* HRTEM and selected area electron diffraction (SAED) analyses. For accurate analyses, we used structural information obtained from the Inorganic Crystal Structure Database (ICSD). As shown in Fig. 8a–c, while the discharged sample exhibited (*hkl*) planes and *d*-spacing corresponding to metallic Cu^0 and K_2SO_4 phases, the (*hkl*) planes and *d*-spacing of the CuSO_4 phase were observed for both the as-prepared and charged sample, which agrees well with the *operando/ex situ* XRD data. To confirm the species formed during the conversion reaction of the CuSO_4 phase in N-CSO/C, we performed ToF-SIMS analyses (Fig. 8d–f). Before the ToF-SIMS measurement, the surface was etched using Ga^+ for 10 s to eliminate the organic contaminants composed of C–H–O bonds from the electrolyte or air. For the as-prepared electrode, only the CuSO_3^+ fragment indicating Cu–S–O bonds (such as CuSO_4) was strongly observed, whereas the other peaks were negligible. After fully discharging to 1.1 V, the CuSO_3^+ fragment was diminished and hardly observed; however, the fragments of KSO_2^- ($m = 102.92$) and Cu^+ ($m = 62.93$) grew sharply, corresponding to K–S–O bonds (such as K_2SO_4) and metallic Cu^0 , respectively. Although the Cu^+ fragment was observed for the as-prepared electrode owing to the

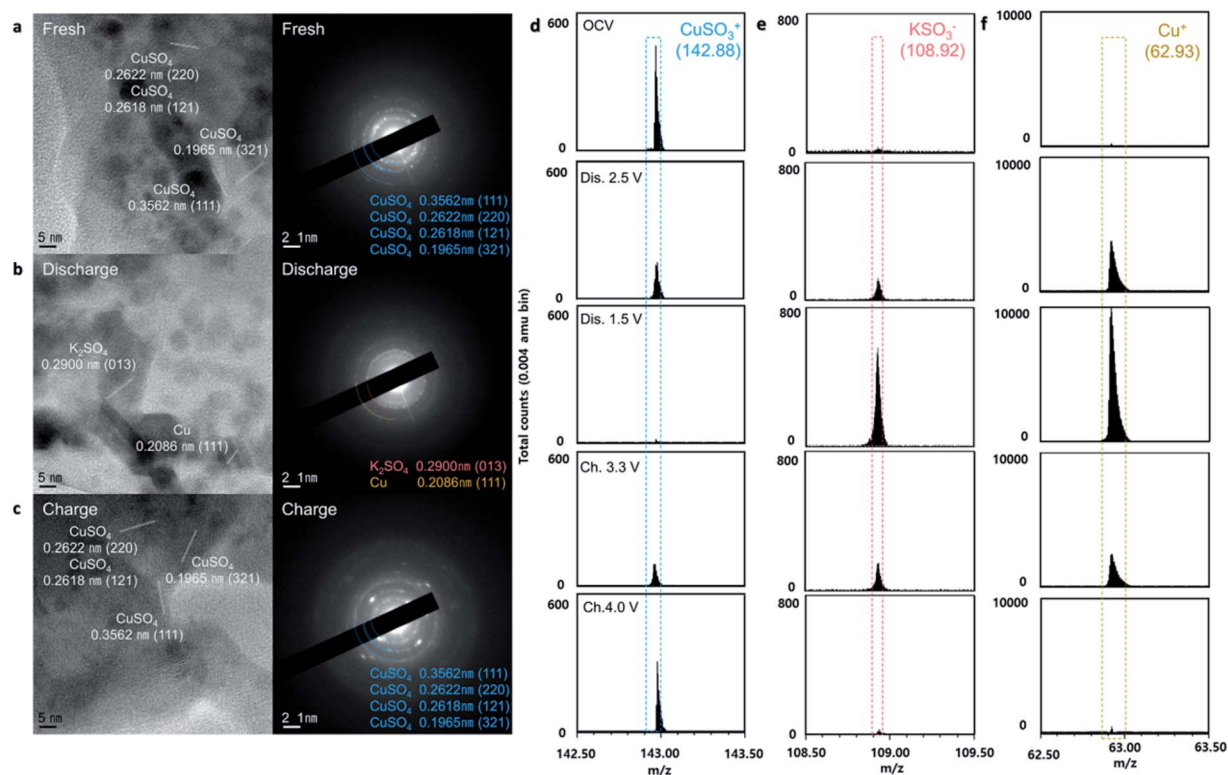


Fig. 8 HRTEM images and SAED patterns of the (a) fresh, (b) discharged, and (c) charged N-CSO/C composite. ToF-SIMS plots of (d) CuSO_3^+ , (e) KSO_3^- and (f) Cu^+ after de/potassium.

presence of the Cu element in CuSO_4 , the evidence was faint at that time; however, the fragment substantially grew at the end of discharge. Thus, it is reasonable to conclude that metallic Cu was formed at the N-CSO/C electrode as discharge proceeded. After fully charging to 4.1 V, the fragments of K_2SO_4 and Cu^+ disappeared and the CuSO_3^+ fragment was recovered, implying the restoration of the CuSO_4 phase. These *ex situ* ToF-SIMS results indicating the conversion reaction of the CuSO_4 phase in the PRB system are consistent with the *operando/ex situ* XRD and HRTEM analyses. In addition, to identify the relationship between Cu^0 formation and K^+ ion transmission, we performed electrochemical impedance spectroscopy (EIS) analyses on fully charged and fully discharged N-CSO/C electrodes in the PRB system. As presented in Fig. S12 (ESI[†]), the charge-transfer resistance of the fully charged sample was larger than that of the fully discharged sample, which indicates that the existence of the metallic Cu^0 phase can affect the K^+ ion transmission. The effect of metallic Cu^0 phases on alkali-ion transmission is similar with that in previous research on the Cu-based conversion-based electrode materials such as CuO and CuS.^{51,52}

4 Conclusions

We proposed a method to develop novel conversion-based cathode materials with ultrahigh energy densities for PRBs. Through a simple high-energy ball-milling process, we successfully prepared N-CSO/C, and the overall reaction mechanism of the CuSO_4 phase in N-CSO/C in the PRB system was

confirmed through combined studies using first-principles calculation and various experimental techniques including *operando/ex situ* XRD, HRTEM, ToF-SIMS, XANES spectroscopy, and EXAFS spectroscopy. N-CSO/C delivered a capacity of $\sim 240 \text{ mA h g}^{-1}$ with an average operating voltage of $\sim 2.8 \text{ V}$ (vs. K^+/K) at 12 mA g^{-1} , resulting in a larger energy density than that of other reported cathode materials for PRBs to date. This exceptionally large energy density of N-CSO/C results from the high operating voltage of the conversion reaction ($\text{CuSO}_4 + 2\text{K}^+ + 2\text{e}^- \leftrightarrow \text{Cu} + \text{K}_2\text{SO}_4$) achieved *via* the inductive effect of sulfur-based polyanions with high electronegativity. In particular, N-CSO/C exhibited not only outstanding power-capability and cyclability but also great full-cell performance when paired with a potassiated hard-carbon anode, implying that it is reasonable to apply N-CSO/C as a cathode in practical PRBs. We believe that this research on N-CSO/C provides fundamental information on conversion-reaction-based cathode materials for not only PRBs but also other rechargeable batteries.

Conflicts of interest

There are no conflicts to declare.

Acknowledgements

This research was supported by the National Research Foundation of Korea funded by the Ministry of Science and ICT of Korea (NRF-2019M2A2A6A05102365, NRF-

2018K2A9A2A12000230, NRF-2020M2D8A2070870). Also, this work was supported by the Primary Research Program (20A01024) of the Korea Electrotechnology Research Institute and by the Korea Institute of Materials Science (KIMS) of the Republic of Korea (PNK6650).

References

- 1 D. Larcher and J. M. Tarascon, *Nat. Chem.*, 2015, **7**, 19–29.
- 2 M. Armand and J. M. Tarascon, *Nature*, 2008, **451**, 652–657.
- 3 J. M. Tarascon and M. Armand, *Nature*, 2001, **414**, 359–367.
- 4 L. L. Wang, B. B. Chen, J. Ma, G. L. Cui and L. Q. Chen, *Chem. Soc. Rev.*, 2018, **47**, 6505–6602.
- 5 B. Dunn, H. Kamath and J. M. Tarascon, *Science*, 2011, **334**, 928–935.
- 6 Y. Zhong, X. H. Xia, F. Shi, J. Y. Zhan, J. P. Tu and H. J. Fan, *Adv. Sci.*, 2016, **3**, 1500286.
- 7 V. Palomares, M. Casas-Cabanas, E. Castillo-Martinez, M. H. Han and T. Rojo, *Energy Environ. Sci.*, 2013, **6**, 2312–2337.
- 8 H. Vikstrom, S. Davidsson and M. Hook, *Appl. Energy*, 2013, **110**, 252–266.
- 9 R. Rajagopalan, Y. G. Tang, X. B. Ji, C. K. Jia and H. Y. Wang, *Adv. Funct. Mater.*, 2020, **30**, 1909486.
- 10 S. J. Wang, P. Xiong, X. Guo, J. Q. Zhang, X. C. Gao, F. Zhang, X. Tang, P. H. L. Notten and G. X. Wang, *Adv. Funct. Mater.*, 2020, **30**, 202001588.
- 11 Z. Zhang, Y. Du, Q. -C. Wang, J. Xu, Y. -N. Zhou, J. Bao, J. Shen and X. Zhou, *Angew. Chem., Int. Ed.*, 2020, **59**, 17504–17510.
- 12 I. Sultana, T. Ramireddy, M. M. Rahman, Y. Chen and A. M. Glushenkov, *Chem. Commun.*, 2016, **52**, 9279–9282.
- 13 C. D. Wessells, S. V. Peddada, R. A. Huggins and Y. Cui, *Nano Lett.*, 2011, **11**, 5421–5425.
- 14 Z. Jian, W. Luo and X. Ji, *J. Am. Chem. Soc.*, 2015, **137**, 11566–11569.
- 15 A. Eftekhari, Z. L. Jian and X. L. Ji, *ACS Appl. Mater. Interfaces*, 2017, **9**, 4404–4419.
- 16 Y. Hironaka, K. Kubota and S. Komaba, *Chem. Commun.*, 2017, **53**, 3693–3696.
- 17 X. P. Wang, X. M. Xu, C. J. Niu, J. S. Meng, M. Huang, X. Liu, Z. Liu and L. Q. Mai, *Nano Lett.*, 2017, **17**, 544–550.
- 18 X. Ge, S. Liu, M. Qiao, Y. Du, Y. Li, J. Bao and X. Zhou, *Angew. Chem., Int. Ed.*, 2019, **58**, 14578–14583.
- 19 T. Masese, K. Yoshii, M. Kato, K. Kubota, Z. D. Huang, H. Senoh and M. Shikano, *Chem. Commun.*, 2019, **55**, 985–988.
- 20 X. P. Wang, P. Hu, C. J. Niu, J. S. Meng, X. M. Xu, X. J. Wei, C. J. Tang, W. Luo, L. Zhou, Q. Y. An and L. Q. Mai, *Nano Energy*, 2017, **35**, 71–78.
- 21 C. L. Liu, S. H. Luo, H. B. Huang, Y. C. Zhai and Z. W. Wang, *Chem. Eng. J.*, 2019, **356**, 53–59.
- 22 Y. Wu, H. B. Huang, Y. Z. Feng, Z. S. Wu and Y. Yu, *Adv. Mater.*, 2019, **31**, 1901414.
- 23 J. H. Deng, X. L. Huang, M. Wang and M. W. Xu, *Mater. Lett.*, 2020, **262**, 127048.
- 24 S. Yu, S. O. Kim, H. S. Kim and W. Choi, *Int. J. Energy Res.*, 2019, **43**, 7646–7654.
- 25 X. Zhang, Y. Huang, S. Wu, Y. Zeng, M. Yu, F. Cheng, X. Lu and Y. Tong, *Acta Phys.-Chim. Sin.*, 2018, **34**, 219–226.
- 26 Y. Kawabe, N. Yabuuchi, M. Kajiyama, N. Fukuhara, T. Inamasu, R. Okuyama, I. Nakai and S. Komaba, *Electrochem. Commun.*, 2011, **13**, 1225–1228.
- 27 N. Recham, J. N. Chotard, L. Dupont, K. Djellab, M. Armand and J. M. Tarascon, *J. Electrochem. Soc.*, 2009, **156**, A993–A999.
- 28 J. Kim, G. Yoon, H. Kim, Y.-U. Park and K. Kang, *Chem. Mater.*, 2018, **30**, 3683–3689.
- 29 A. K. Padhi, K. S. Nanjundaswamy and J. B. Goodenough, *J. Electrochem. Soc.*, 1997, **144**, 1188–1194.
- 30 C. Liu, Z. G. Neale and G. Cao, *Mater. Today*, 2016, **19**, 109–123.
- 31 P. Barpanda, G. Oyama, S. Nishimura, S. C. Chung and A. Yamada, *Nat. Commun.*, 2014, **5**, 4358.
- 32 Y. G. Wang, Y. R. Wang, E. J. Hosono, K. X. Wang and H. S. Zhou, *Angew. Chem., Int. Ed.*, 2008, **47**, 7461–7465.
- 33 H. H. Lyu, B. Gao, F. He, C. Ding, J. C. Tang and J. C. Crittenden, *ACS Sustainable Chem. Eng.*, 2017, **5**, 9568–9585.
- 34 X. D. Liu, H. T. Liu, Y. M. Zhao, Y. Z. Dong, Q. H. Fan and Q. Kuang, *Langmuir*, 2016, **32**, 12593–12602.
- 35 I. Almodovar, B. C. Frazer, J. J. Hurst, D. E. Cox and P. J. Brown, *Phys. Rev.*, 1965, **138**, A153–A155.
- 36 J. U. Choi, J. Kim, J. H. Jo, H. J. Kim, Y. H. Jung, D. C. Ahn, Y. K. Sun and S. T. Myung, *Energy Storage Mater.*, 2020, **25**, 714–723.
- 37 C. Vaalma, G. A. Giffin, D. Buchholz and S. Passerini, *J. Electrochem. Soc.*, 2016, **163**, A1295–A1299.
- 38 J. H. Jo, J. U. Choi, Y. J. Park, Y. H. Jung, D. Ahn, T. Y. Jeon, H. Kim, J. Kim and S. T. Myung, *Adv. Energy Mater.*, 2020, **10**, 1903605.
- 39 J. Y. Hwang, J. Kim, T. Y. Yu, S. T. Myung and Y. K. Sun, *Energy Environ. Sci.*, 2018, **11**, 2821–2827.
- 40 H. Kim, J. C. Kim, S. H. Bo, T. Shi, D. H. Kwon and G. Ceder, *Adv. Energy Mater.*, 2017, **17**, 1700098.
- 41 T. Deng, X. L. Fan, C. Luo, J. Chen, L. Chen, S. Hou, N. Eidson, X. Q. Zhou and C. S. Wang, *Nano Lett.*, 2018, **18**, 1522–1529.
- 42 J. H. Jo, J. Y. Hwang, J. U. Choi, H. J. Kim, Y. K. Sun and S. T. Myung, *J. Power Sources*, 2019, **432**, 24–29.
- 43 C. Zhang, Y. Xu, M. Zhou, L. Liang, H. Dong, M. Wu, Y. Yang and Y. Lei, *Adv. Funct. Mater.*, 2017, **27**, 1604307.
- 44 J. Zhang, Z. Cao, L. Zhou, G. Liu, G. T. Park, L. Cavallo, L. Wang, H. N. Alshareef, Y. K. Sun and J. Ming, *ACS Energy Lett.*, 2020, **5**, 2651–2661.
- 45 J. Y. Hwang, J. Kim, T. Y. Yu, H. G. Jung, J. K. Kim, K. H. Kim and Y. K. Sun, *J. Mater. Chem. A*, 2019, **7**, 21362–21370.
- 46 J. U. Choi, Y. J. Park, J. H. Jo, Y. H. Jung, D. C. Ahn, T. Y. Jeon, K. S. Lee, H. S. Lee, S. S. Lee, J. Kim and S. T. Myung, *Energy Storage Mater.*, 2020, **27**, 342–351.
- 47 X. Fan, C. Luo, J. Lamb, Y. Zhu, K. Xu and C. Wang, *Nano Lett.*, 2015, **15**, 7650–7656.

- 48 Y.-Z. Wang, X.-Y. Shan, D.-W. Wang, Z.-H. Sun, H.-M. Cheng and F. Li, *Joule*, 2018, **2**, 1278–1286.
- 49 J. A. Rodriguez, J. C. Hanson, D. Stacchiola and S. D. Senanayake, *Phys. Chem. Chem. Phys.*, 2013, **15**, 12004–12025.
- 50 E. B. Fox, S. Velu, M. H. Engelhard, Y. H. Chin, J. T. Miller, J. Kropf and C. S. Song, *J. Catal.*, 2008, **260**, 358–370.
- 51 Q. Su, L. Yao, J. Zhang, G. Du and B. Xu, *ACS Appl. Mater. Interfaces*, 2015, **7**, 23062–23068.
- 52 M. Wu, Y. Zhang, T. Li, Z. Chen, S. Cao and F. Xu, *Nanoscale*, 2018, **10**, 12526.